

Fracture Toughness and Fracture Roughness in Anisotropic Granitic Rocks

M. H. B. Nasseri · G. Grasselli · B. Mohanty

Received: 13 March 2008 / Accepted: 7 October 2009 / Published online: 17 November 2009
© Springer-Verlag 2009

Abstract In this paper we present an experimental approach aimed at assessing the correlation between fracture toughness (K_{IC}) and fracture roughness of two granitic rocks (Barre and Stanstead granites) exhibiting significant fracture toughness anisotropy. Roughness values have been estimated for fractured surfaces obtained from Chevron Cracked Notch Brazilian Disc samples failed under mode I along three orthogonal planes with respect to their microstructural fabrics. There exists a clear correlation between roughness and toughness within each rock examined along the three planes. Specific orientation of micro-crack alignment could result in preferred out-of-plane propagation of the test-crack irrespective of grain-size distribution. These experimental observations reinforce the hypothesis of the existence of a link among pre-existing petrofabric anisotropy, fracture toughness, fracture roughness, and the evolution and extent of the associated induced fractures within the process zone of granitic rocks along specific directions. This study also highlights the need for employment of pre-failure and advanced post-failure diagnostic techniques in quantifying these interrelationships.

Keywords Fracture toughness · Fracture roughness · X-ray micro CT · SEM · Fracture process zone

1 Introduction

Preferentially oriented microstructural fabric and microcracks in granitic rocks are largely responsible for their anisotropic properties. In a previous attempt to study the fracture toughness anisotropy and its relation to the microstructural fabrics in granitic rocks (Nasseri and Mohanty 2008; Nasseri et al. 2006), it was concluded that fracture toughness is highly sensitive to the presence of oriented microcracks. The measured fracture toughness anisotropy was also found to have good correlation with measured differences in seismic velocities. The study showed that the measured values of fracture toughness can show differences ranging up to 2.4 times for the same rock type. This anisotropy has been linked directly to the microstructural anisotropy present in the rock, as represented by the size of dominant microstructural fabric, and its orientation with respect to the direction of propagation of the induced fracture (test-crack). For instance, when a test-crack propagates at right angle to the dominant preferred microstructural fabric, it yields the higher fracture toughness value. The produced test-crack, when observed in a thin section, is characterized by increasing segmentation (sudden termination and reappearance of test-crack) and higher deflection (deviation from main direction) that result in a more tortuous profile (see Fig. 14a in Nasseri and Mohanty 2008). In contrast, when the test-crack is forced to propagate parallel to the dominant preferred microstructural fabric, this yields the lower fracture toughness value. The profile of such a test-crack, when observed under thin section, is smooth and does not show deflection (see Fig. 14b in Nasseri and Mohanty 2008). A large number of studies have tried to quantify fracture roughness of such failed surfaces tested under mode I; however, only limited attempts have been made in the past

M. H. B. Nasseri (✉) · G. Grasselli · B. Mohanty
Department of Civil Engineering, Lassonde Institute,
University of Toronto, Toronto, ON, Canada
e-mail: Nasseri@ecf.utoronto.ca

to characterize such fracture surfaces and to correlate the fracture roughness with fracture toughness (Backers et al. 2003; Issa et al. 2003; Lange et al. 1993) in rocks. These findings confirm that as fracture toughness increases, the surface roughness of the fracture generated, expressed as a function of its fractal dimension, increases.

The present study investigates the correlation between the anisotropy in fracture toughness, obtained under mode I (Iqbal and Mohanty 2006; ISRM 1995) and that measured in fracture surface roughness, evaluated with the methodology proposed by Grasselli et al. (2002) for Barre and Stanstead granites. Post-failure techniques, such as petrographical, SEM, stereo-topometric, and 3D-microCT scanning have been used to understand the interrelationship between pre-existing microstructural fabric and induced crack geometry in Barre and Stanstead granites.

2 Experimental Setup and Procedure

2.1 Microstructural Investigation and Sample Selection

To collect information regarding natural *in situ* orientation of the granitic blocks and internal rock fabric, thin sections

($3.5 \text{ cm} \times 2.2 \text{ cm}$) were prepared normal to three chosen orthogonal axes along which P-wave velocities were measured. Intermediate, slow, and fast directions were assigned X, Y, and Z axes, respectively (Figs. 1, 2). Optical microstructural analysis of the two granitic rocks detailed the variation in terms of mineral size distribution, mineral shape, microcrack, and their preferred orientation (Tables 1, 2). In our analysis one screen pixel represented $1 \mu\text{m}$. Thus the shortest resolvable crack and grain size had a cutoff limit of approximately $1 \mu\text{m}$. In this investigation we set the cutoff limit for the crack and grain size analysis to be $100 \mu\text{m}$. In order to distinguish the induced cracks from the pre-existing ones in and around the test-crack (process zone), SEM imaging of the thin sections was carried out ($\times 2,000$ magnification) and compared to similar measurements previously done on thin sections prepared from intact rock. “Intercept” and “SPO” (Launeau and Robin 1996) programs were used to calculate optical microcrack densities and determine the mineral size distribution and shape ratio.

2.1.1 Barre Granite

Barre granite is part of the Devonian New Hampshire pluton series located in the south-west region of Burlington in the

Fig. 1 3D block diagram showing microcrack orientations in Barre granite; rose diagrams show the alignment of microcracks and mineral fabric orientation for each plane. Fracture toughness and fracture roughness were measured along K_{xy} , K_{zy} , and K_{xz} . The first index after K represents the direction of an axis perpendicular to the failed plane, and the second index indicates the direction parallel to the tip of the machined notches in that plane. The box on the right side of the figure shows the plan and section view for K_{xz} , where the first index (x) is the direction of the axis perpendicular to the failed plane (YZ) and the second index (z) shows the direction parallel to the tip of the notches along Z axis. XY plane is considered to be parallel to the rift plane, YZ plane is parallel to grain plane, and XZ plane runs parallel with hard way plane in Barre granite

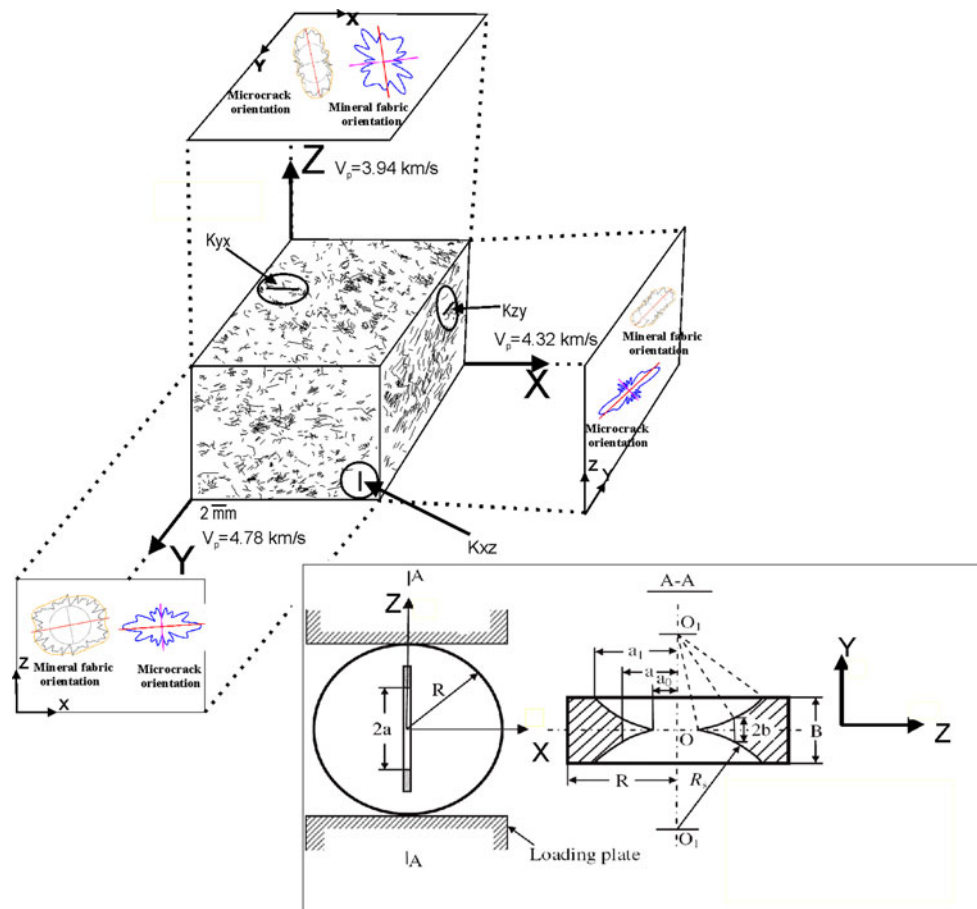
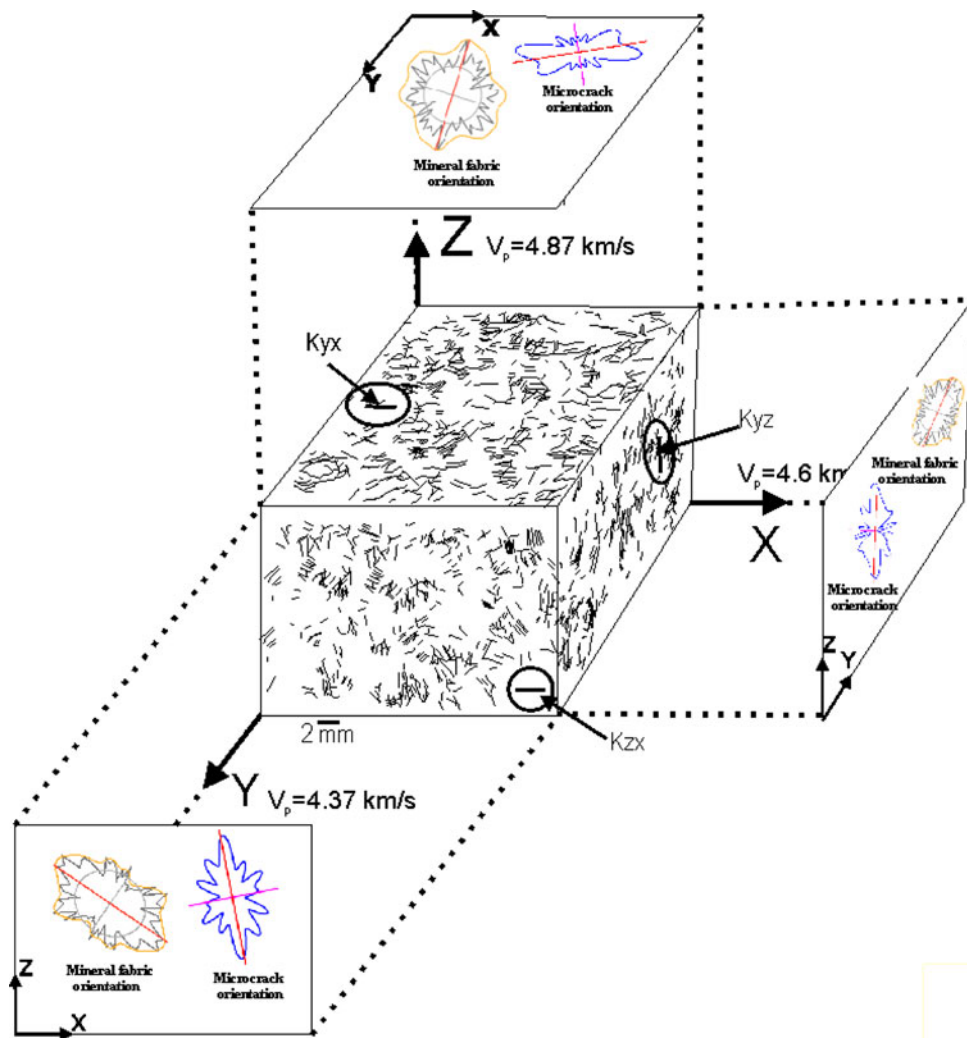


Fig. 2 3D block diagram showing microcracks orientations in Stanstead granite; rose diagrams show the alignment of microcracks and mineral fabric orientation for each plane, i.e. XY (hard way), XZ (rift), and YZ (grain) planes. Fracture toughness and fracture roughness were measured along Kyx, Kzx, and Kyz. The first index after K represents the direction of an axis perpendicular to the failed plane, and the second index indicates the direction parallel to the tip of the machined notches in that plane



state of Vermont, USA. It is a gray medium to fine-grained granodiorite characterized by a very consistent composition that consists of 35% oligoclase feldspar, 21% microcline feldspar, 9% biotite mica, 27% quartz and 6% muscovite mica, and various accessory minerals. Its mineral grain size ranges from 0.25 to 3 mm. The samples used in this study are characterized by having quartz grains with an average size of 0.94 mm. The average feldspar grain size is 0.95 mm, and the corresponding average biotite grain size is 0.43 mm (Table 1). The microcracks are of intragranular to intergranular type and are found in both quartz and feldspar grains and along cleavage planes of biotite grains. Table 2, shows the grain size distribution and relevant grain shape ratio measured along the three orthogonal planes discussed in this work. The mineral grain shape has a ratio of 1.26, 1.07, and 1.25 along XY (rift), XZ (hard way), and YZ (grain) planes, respectively (Table 2). As is evident from the 3D block diagram of microcrack orientation in Fig. 1, microcrack orientation in Barre granite is preferably oriented

within the rift plane (XY, plane of easiest splitting), traces of which are clearly shown as microcracks parallel to Y on YZ and to X axes on XZ planes. On the YZ plane the larger microcracks (2–3 mm long) are seen to run parallel to Y axis cutting through the larger quartz grains and the shorter ones (~ 1 mm) run parallel to Z axis. The XY plane is parallel to the rift plane for Barre granite in this study and shows microcrack density of 5.2 cm/cm^2 calculated over the thin section area. The average microcrack length observed on the XY, XZ, and YZ planes are 0.84 ± 0.36 , 0.68 ± 0.25 , and 1.07 ± 0.54 mm, respectively (Table 2). The rose diagrams representing the pre-existing (intact rock) microcrack and mineral fabric orientation along specific directions for each plane are shown in Fig. 1.

2.1.2 Stanstead Granite

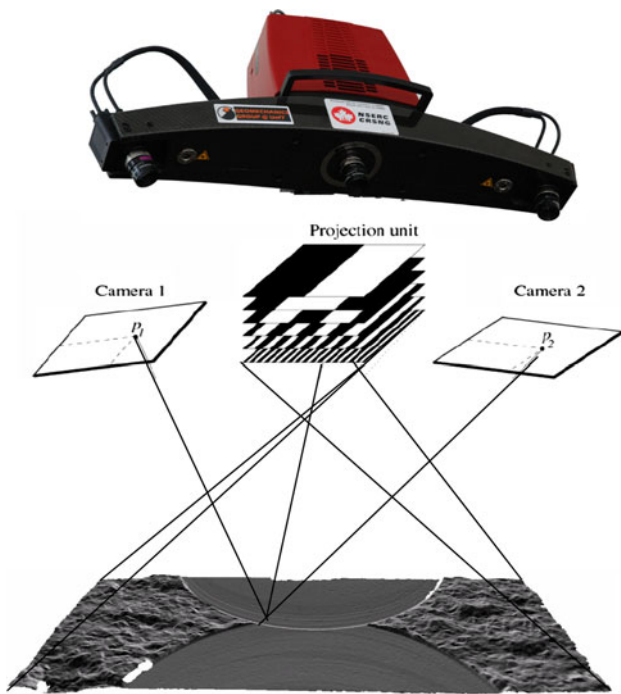
Stanstead granite comes from the Beebe region of eastern township in Quebec near the border with the USA. This

Table 1 Mineral composition of the rocks studied

Planes	Parameters					
	Average grain		Average grain		Average grain	
	Size (mm)	%	Size (mm)	%	Size (mm)	%
Barre granite	Quartz		Feldspar		Biotite	
XY plane	0.93	25	1.10	65	0.46	6
XZ plane	0.95	31	0.81	61	0.43	6
YZ plane	0.94	31	0.96	65	0.40	4
Stanstead granite	Quartz		Feldspar		Biotite	
XY plane	1.25	25	1.40	65	0.60	10
XZ plane	1.30	23	1.63	68	0.62	9
YZ plane	1.20	26	1.45	67	0.60	7

rock is of Devonian age and its color varies from white to a dark gray depending on its mica content. It is a fine to coarse-grained rock with mineral composition of 65% feldspar, 25% quartz, and 8.5% of biotite. Its mineral grain size ranges from 0.25 to 4.5 mm. The average quartz grain size is 1.25 mm. The average feldspar grain size is 1.49 mm and the average biotite grain size in this rock is 0.61 mm (Table 1). The microcracks in this rock are of intragranular to intergranular type and are found in both quartz and feldspar grains and along cleavage planes of biotite grains. The microcracks are generally larger than what was observed in Barre granite.

The mineral grain shape has a ratio of 1.03, 1.12, and 1.21 along XY (hard way), YZ (grain), and XZ (rift) planes, respectively (Table 2). As is evident from the 3D block diagram of microcrack orientation in Fig. 2, the larger microcracks (2–3.5 mm) are seen to run nearly parallel to the X axis and the shorter ones (~ 1 mm) run nearly parallel to Y axis on the XY plane. This plane exhibits the highest microcrack density of $5.2 \text{ cm}/\text{cm}^2$ in comparison with the other two planes (Table 2). The

**Fig. 3** Stereo-topometric scanner used to digitize surface roughness

average microcrack length observed on XY, XZ, and YZ planes are 1.38 ± 0.52 , 1.08 ± 0.45 , and 0.94 ± 0.41 mm, respectively. The rose diagrams representing the directions of the pre-existing microcracks (microcracks present in the sample before testing it) and mineral petro-fabric orientation for the three planes are shown to be unidirectional as demonstrated in Fig. 2.

2.2 Fracture Roughness: Measurement Techniques and Procedure

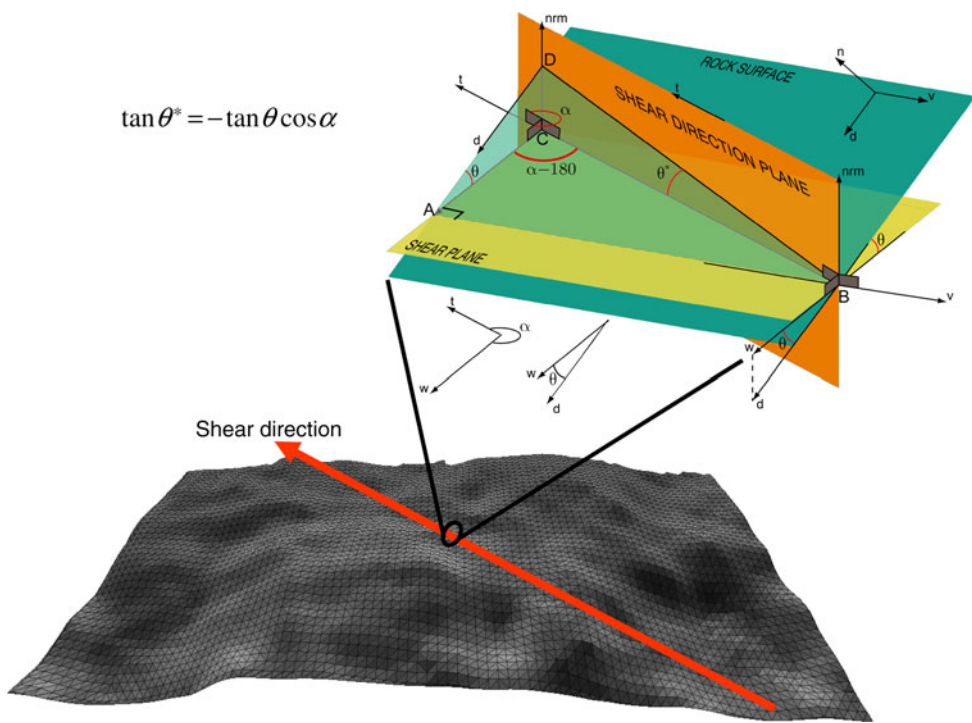
Quantification of fracture roughness is a very challenging problem common to many different disciplines. In this work

Table 2 Microstructural features of the rocks studied

Planes	Parameters					
	Average grain shape			No. grain	$\phi (\text{cm}/\text{cm}^2)$	Average μ crack length (mm)
	(a) (mm)	(b) (mm)	(a/b)			
Barre granite						
XY plane (rift)	1.41	1.12	1.26	972	5.20	0.84 ± 0.3
XZ plane (hard way)	1.08	1.00	1.07	1,534	4.46	0.68 ± 0.25
YZ plane (grain)	1.38	1.10	1.25	1,138	4.10	1.07 ± 0.54
Stanstead granite						
XY plane (hard way)	1.17	1.14	1.03	893	5.20	1.38 ± 0.52
XZ plane (rift)	1.35	1.11	1.21	668	4.80	1.08 ± 0.45
YZ plane (grain)	1.28	1.13	1.12	771	2.80	0.94 ± 0.41

(a) = Ellipsoid's long axis, (b) = Ellipsoid's short axis, ϕ = microcrack density

Fig. 4 Geometrical identification of the apparent dip angle θ^* , measured along a chosen direction (shear direction) with respect to the fracture average plane (shear plane) (Grasselli et al. 2002)



roughness has been evaluated using the methodology proposed by Grasselli et al. (2002) and Grasselli (2006). The surface data have been acquired using a 3D stereo-topometric measurement system (ATOS). Such a system offers both the advantages of high precision and good repeatability, as well as being fast and easy to use since it is able to digitize the entire surface at once (Grasselli 2001). The system works on a novel principle compared to one-camera fringe projection sensors. Various white-light fringe patterns are projected onto the object surface and recorded by two digital cameras, which are integrated into the measurement head, from two different angles (Fig. 3). 3D coordinates are computed independently with high accuracy for each of the camera pixels using triangulation methods and digital image processing (fringe projection and image shifting). Consistent exploitation of redundant information minimizes the measurement errors. Due to the high data density resulting from the optical measurement process, details of the rough surface can be depicted precisely. For the set-up chosen for this study we measured points on a 250-μm xy grid. The accuracy of the spatial location of each point in the 3D space (point cloud) along the z direction has been computed to be ±20 μm. For the current research, the fractured surfaces were reconstructed from the 3D point clouds with a specially developed triangulation algorithm (Wirth 2002). This approach results in a discretization of the fracture surface into contiguous triangles, defined by vertices and by the orientation of the vector normal to the plane of the triangle. Looking at the reconstructed surface, each triangle orientation is uniquely identified by its Azimuth

angle (α) and dip angle (θ) (Fig. 4). As presented in detail by Grasselli et al. (2002) and Grasselli (2006), it is possible to describe the fracture surface roughness as function of the apparent dip angle (θ^*), which quantifies “how steep” each triangle is with respect to the fracture average plane, measured along a chosen direction (Fig. 4). For each surface it is possible to calculate the area of the joint that has an apparent dip angle equal to or greater than a chosen threshold dip angle. The cumulative area is then normalized with respect to the total area of the fracture, and it is termed A_{θ^*} . By varying the threshold dip value from 0 degrees to the maximum apparent dip angle (θ_{\max}^*) measured on the surface, it is possible to plot the variation of A_{θ^*} as function of the threshold dip angle (Fig. 5). The relationship between the A_{θ^*} and the θ^* can be described by the following equation (see Grasselli et al. 2002 for more details):

$$A_{\theta^*} = A_0 \left(\frac{\theta_{\max}^* - \theta^*}{\theta_{\max}^*} \right)^C \quad (1)$$

where A_0 is the percentage of the fracture area having an apparent dip angle of 0 degrees or higher in the direction analyzed, θ_{\max}^* is the maximum apparent dip angle in the direction analyzed, and C is a “roughness” parameter, calculated using a best-fit regression function, which characterizes the distribution of the apparent dip angles over the surface with respect to the direction analyzed (Grasselli et al. 2002). As discussed in detail by Grasselli (2006), the parameters A_0 , C , and θ_{\max}^* depend on the specified direction that is analyzed, as well as on the 3D surface representation (i.e. triangulation algorithm and

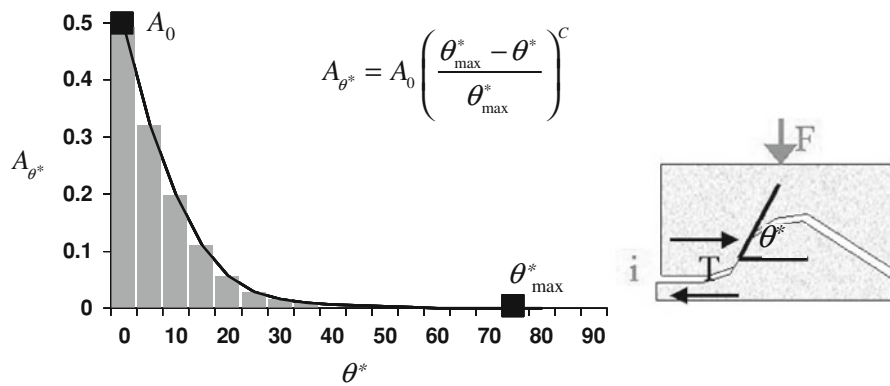
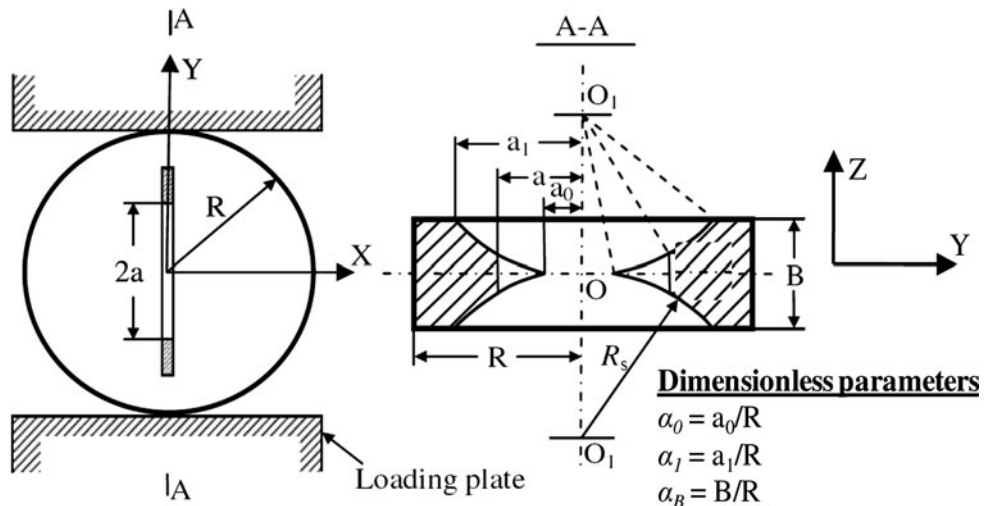


Fig. 5 This plot describes, for a given shear direction, the distribution of the cumulative area of the surface A_{θ^*} characterized by an apparent dip angle (θ^*) equal or greater than a chosen threshold value. θ^* is measured with respect to the average plane of the joint. As

evident from the figure, increasing the threshold value θ^* , the value of cumulative area of the surface A_{θ^*} rapidly decreases. It has been experimentally proven that such decay can be described by the above power law (Grasselli 2006)

Fig. 6 Geometry of the CCNBD and related parameters (after ISRM 1995). R radius of disc, B thickness of disc, R_s radius of saw, a length of crack, a_0 initial half length of chevron notch, a_1 final half length of chevron notch. K_{xy} is used to identify the plane along which the fracture toughness is determined. The first index (x) in this example represents the direction of the axis normal to the tested plane, and the second index (y) indicates the direction of an axis which is parallel to the tip of the notches (Nasseri and Mohanty 2008)



measurement resolution). In order to visualize the surface roughness anisotropy, the parameters A_0 , C , and θ_{\max}^* are calculated along several possible directions, and the values of ratio θ_{\max}^*/C , obtained for each of those, can be plotted in a polar diagram (Grasselli 2006).

2.3 Fracture Toughness Measurements

In the present study we use the Chevron Cracked Notch Brazilian Disc (CCNBD) test method (Fig. 6) to study the anisotropy in fracture toughness (highest K_{IC} /lowest K_{IC} within the same rock) in Barre and Stanstead granites (Nasseri and Mohanty 2008). The Brazilian disc samples were prepared from three chosen orthogonal planes representing rift, grain, and hard way of Barre and Stanstead granites (Figs. 1, 2). P-wave velocity measurements perpendicular to those planes showed similar trend, having the lowest value recorded perpendicular to the rift plane (see XY plane in Fig. 1 and XZ plane in Fig. 2), the highest

value perpendicular to the hard way plane (see XZ plane in Fig. 1 and XY plane in Fig. 2), and an intermediate value for the grain plane (see YZ plane in Fig. 1 and YZ plane in Fig. 2). 3D blocks containing mapped microstructural fabric (Figs. 1, 2) were developed using CorelDraw software based on analysis of thin sections that were made perpendicular to the three axes along which P-wave velocities were measured. Figure 7 shows the variation of fracture toughness experimental data (Fig. 7a, b), mean and its standard deviations (Fig. 7c) measured along these different planes for Barre and Stanstead granite.

As described in detail in the ISRM suggested method and by Iqbal and Mohanty (2006), the fracture toughness K_{IC} can be evaluated as

$$K_{IC} = \frac{P_{\max}}{B\sqrt{R}} Y_{\min}^* \quad (2)$$

where P_{\max} is the maximum load at failure, B is the disc's thickness, R is the radius of the disc, and Y_{\min}^* is a critical

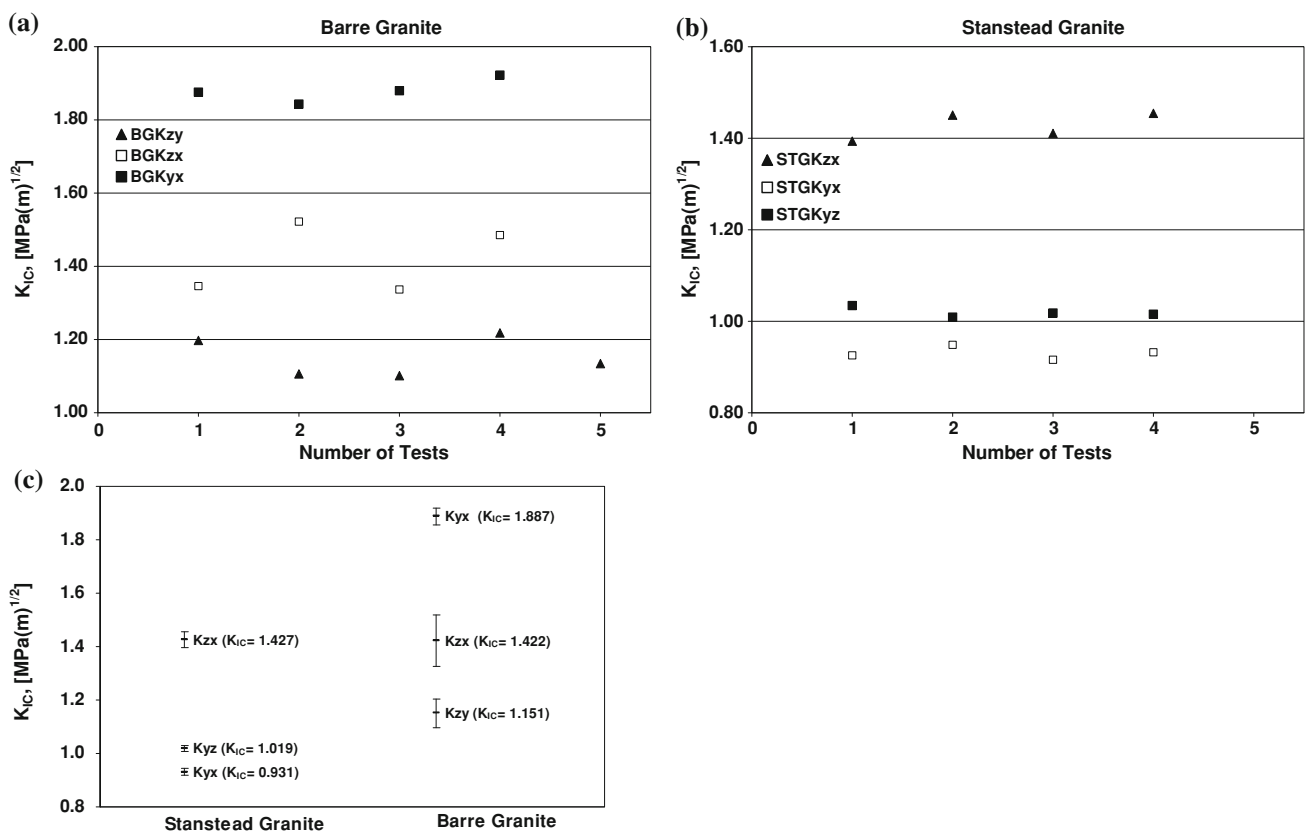


Fig. 7 **a** Variation of fracture toughness (three different directions) for Barre granite. **b** Variation of fracture toughness (three different directions) for Stanstead granite. **c** Average variation of fracture toughness (three different directions) for Barre and Stanstead granites.

dimensionless stress intensity value for the specimen, which is determined by the specimen geometry dimensions α_0 , α_1 , and α_B (shown in Fig. 6 and ISRM suggested method for CCNBD, 1995), and is defined as

$$Y_{\min}^* = \mu \cdot e^{Y \cdot \alpha_1} \quad (3)$$

where μ and Y are constants determined by α_0 , α_B , following the procedure reported in the ISRM suggested method for CCNBD, 1995. All used values are provided in Table 3 and shown in Fig. 6.

Notches were machined within the disc specimens, according to the ISRM (1995) suggested method. Using a MTS servo-controlled loading machine and TestStar software, displacement, force, and time base were recorded during testing.

3 Experimental Results

3.1 Fracture Toughness Anisotropy in Barre Granite

Table 3 shows the result for the fracture toughness measured along specific planes for Barre and Stanstead

The *error bars* are equal to one standard deviation calculated from the experimental fracture toughness values associated with each tested direction

granites. Four to five specimens for each plane were tested in order to verify the reproducibility of K_{IC} measurements as a function of petrofabric orientation. Table 3 also shows all the parameters that are required to calculate K_{IC} . Table 4 shows the average K_{IC} values and their standard deviations for the three planes for each rock.

The Barre granite (BG) samples analyzed in this study show a fracture toughness anisotropy (higher K_{IC} /lower K_{IC}) of 1.64. The average fracture toughness for the three planes reported in this study (i.e. K_{yx} , K_{zx} , and K_{zy}) yields K_{IC} values of 1.15, 1.42, and 1.89 (MPa m $^{0.5}$), respectively (Table 4). After the toughness test, thin sections (Fig. 8a-d) containing the fracture profile from the plane characterized with highest and lowest K_{IC} values were made, and processed for SEM analysis. Induced microcrack density and its preferred orientation around the test-crack process zone were measured and shown in (Fig. 9a, b). The rose diagrams in these figures represent the orientation of the induced fractures formed during the propagation of test-crack and the direction of these new fractures within the process zone in Barre granite. When the test-crack propagates parallel to the pre-existing microstructural fabric orientation (Fig. 9a), the damage

Table 3 Fracture toughness experimental results

Sample	Parameters ^a														
	D (mm)	B (mm)	R (mm)	2a ₁ (mm)	α ₀	α _s	α ₁	h _c (mm)	a ₀ (mm)	P (kN)	α _B	μ	Y	Y _{min}	K _{IC} (MPa m ^{0.5})
Fracture toughness (CCNBD) for Barre granite															
Kzy															
Kzy1	75.8	29.5	38	47.2	0.621	0.660	0.253	16.614	9.6	8.640	0.776	0.266	1.766	0.797	1.198
Kzy2	75.8	29.8	38	47.2	0.621	0.660	0.253	16.620	9.6	8.100	0.784	0.266	1.758	0.793	1.106
Kzy3	75.8	30.3	38	47.2	0.621	0.660	0.253	16.620	9.6	8.200	0.797	0.266	1.758	0.793	1.101
Kzy4	75.8	30.4	38	47.2	0.621	0.660	0.224	16.620	8.5	9.100	0.800	0.266	1.758	0.793	1.218
Kzy5	75.8	30.3	38	47.2	0.621	0.660	0.222	16.620	8.45	8.500	0.797	0.265	1.758	0.788	1.134
Kzx															
Kzx1	76	29	38	47.2	0.621	0.658	0.216	16.751	8.2	9.560	0.763	0.266	1.764	0.796	1.346
Kzx2	76	29	38	47.2	0.621	0.658	0.237	16.751	9	10.810	0.763	0.266	1.765	0.796	1.522
Kzx3	76	30	38	47.2	0.621	0.658	0.224	16.751	8.5	9.900	0.789	0.265	1.761	0.790	1.337
Kzx4	76	30	38	47.2	0.621	0.658	0.224	16.751	8.5	11.000	0.789	0.265	1.761	0.790	1.485
Kyx															
Kyx1	76	30.2	38	47	0.618	0.658	0.221	16.471	8.4	14.050	0.795	0.265	1.761	0.786	1.876
Kyx2	76	30.5	38	47	0.618	0.658	0.187	16.471	7.1	14.140	0.803	0.262	1.755	0.775	1.843
Kyx3	76	30.2	38	47	0.618	0.658	0.187	16.471	7.1	14.240	0.795	0.262	1.758	0.777	1.880
Kyx4	76	30.3	38	47	0.618	0.658	0.216	16.471	8.2	14.500	0.797	0.265	1.755	0.783	1.922
Kyx5	76	30.2	38	47	0.618	0.658	0.216	16.471	8.2	14.400	0.795	0.265	1.755	0.783	1.915
Fracture toughness (CCNBD) for Stanstead granite															
Kyx															
Kyx1	76	30.3	38	47.5	0.6250	0.6579	0.2184	17.1938	8.3	6.914	0.797	0.264	1.758	0.791	0.926
Kyx2	76	30.6	38	47.5	0.6250	0.6579	0.2079	17.1938	7.9	7.180	0.805	0.263	1.756	0.788	0.949
Kyx3	76	29.8	38	47.5	0.6250	0.6579	0.2500	17.1938	9.5	6.664	0.784	0.265	1.763	0.798	0.916
Kyx4	76	30.5	38	47.5	0.6250	0.6579	0.2237	17.1938	8.5	6.997	0.803	0.264	1.758	0.792	0.932
Kyz															
Kyz1	76	30.5	38	47.8	0.6289	0.6579	0.2368	17.6658	9	7.664	0.803	0.265	1.761	0.802	1.034
Kyz2	76	30	38	47	0.6184	0.6579	0.2368	16.4706	9	7.497	0.789	0.265	1.761	0.787	1.009
Kyz3	76	30	38	47.1	0.6197	0.6579	0.2368	16.6097	9	7.547	0.789	0.265	1.761	0.789	1.018
Kyz4	76	29.9	38	47.1	0.6197	0.6579	0.2487	16.6097	9.45	7.497	0.787	0.265	1.761	0.789	1.015
Kzx															
Kzx1	76	29	38	47.4	0.6237	0.6579	0.2434	17.0432	9.25	10.246	0.763	0.256	1.764	0.769	1.394
Kzx2	76	29	38	47.4	0.6237	0.6579	0.2763	17.0432	10.5	10.129	0.763	0.269	1.765	0.810	1.451
Kzx3	76	30	38	47.4	0.6237	0.6579	0.2289	17.0432	8.7	11.212	0.789	0.246	1.757	0.736	1.411
Kzx4	76	30	38	47.4	0.6237	0.6579	0.2368	17.0432	9	11.562	0.789	0.246	1.757	0.736	1.455

D diameter of the disc, B thickness of disc, R radius of disc; R_s radius of saw, a_1 final half length of chevron notch, $\alpha_0 = a_0/R$, $\alpha_s = 2R_s/D$, $\alpha_1 = a_1/R$; h_c depth of cut, a_0 initial half length of chevron notch, P load at failure; $\alpha_B = B/R$, μ and Y are constants determined by α_0 , α_B , Y_{\min} calculated from Eq. 3 in the text, K_{IC} fracture toughness

^a These parameters measure the geometry of the CCNBD fractures which are defined in Fig. 4 and ISRM (1995) suggested methods

pattern in its process zone is characterized by long and continuous fractures forming parallel to the direction of propagation. The induced fracture density for the said direction was calculated to be 1.4 mm/mm². The resulting test-crack profile is smooth and does not show major deflection. The rose diagram representing the induced fracture orientation shows single maxima reflecting the dominating direction of the induced fractures running

parallel to the propagation direction within the process zone of Barre granite (Fig. 9a). In contrast, when the test-crack is forced to propagate perpendicular to the pre-existing microstructural fabric, the test-crack is strongly influenced by the presence of pre-existing microstructural fabric orientation that is perpendicular to its propagation. The rose diagram shows indeed two maxima perpendicular to each other reflecting the activation of pre-existing

Table 4 Average values and standard deviations obtained from fracture toughness and fracture roughness measurements

Rock type	Planes/directions	$\langle K_{IC} \rangle$ (MPa m ^{0.5})	STD K_{IC} (MPa m ^{0.5})	$\langle \theta^*/C \rangle$	STD θ^*/C
Barre granite	Kyx	1.887	0.032	9.78	0.82
Barre granite	Kzx	1.422	0.095	8.72	0.37
Barre granite	Kzy	1.151	0.053	8.51	0.68
Stanstead granite	Kzx	1.427	0.030	12.23	1.41
Stanstead granite	Kyz	1.019	0.011	9.57	0.85
Stanstead granite	Kyx	0.931	0.014	9.16	0.75

microcracks and grain boundaries oriented normal to the propagation direction (Fig. 9b). In this case, the induced fracture density is 1.85 mm/mm² within the process zone of Barre granite, which is 30% greater than that measured along the preferred direction.

3.2 Fracture Toughness Anisotropy in Stanstead Granite

The Stanstead granite (STG) samples analyzed in this study show a fracture toughness anisotropy of 1.53. Fracture toughness measured along Kzx shows the highest average value of 1.43 (MPa m^{0.5}), (Table 4) while for Kyx and Kyz average K_{IC} values are considerably reduced: 0.93 and 1.02 (MPa m^{0.5}), respectively. Similar to the characteristic

features of the process zone in Barre granite, Stanstead granite has the highest induced fracture density of 1.56 mm/mm² when the test-crack is forced to propagate normal to the pre-existing preferred microstructural fabric (Fig. 10b). This is about 25% more than what has been measured along the direction in which the test-crack is forced to propagate parallel to the pre-existing microstructural fabric ($\rho = 1.16$ mm/mm²; Fig. 10a). The rose diagram representing the orientation of induced fracture within the process zone of the plane showing the highest fracture toughness has two maxima (Fig. 10b); whereas the rose diagram representing the orientation of induced fractures within the process zone of the plane showing the lowest fracture toughness has a single maximum (Fig. 10a). These rose diagrams represent the orientation of

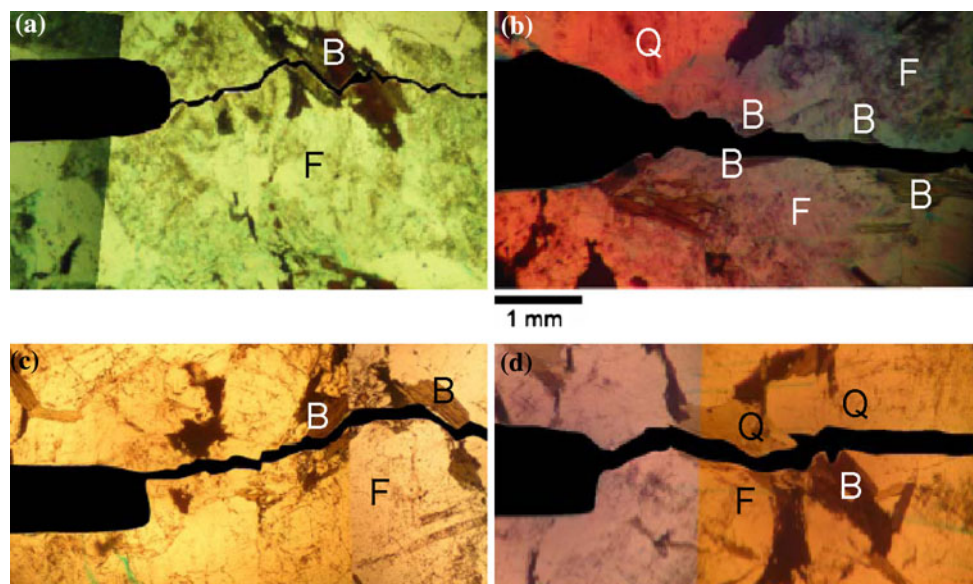


Fig. 8 Thin sections prepared from tested specimens containing the profiles of the test-cracks in Barre and Stanstead granites. **a** Showing the test-crack issuing from the tip of the notch (left-hand side of the image) propagating perpendicular to pre-existing microstructural fabric orientation in Barre granite; note the deflection of the test-crack by the cleavage planes within the biotite. **b** The test-crack propagating parallel to the pre-existing microstructural fabric orientation in Barre granite; note the test-crack splitting through the biotite mineral cleavage planes on its either side of the test-crack. **c** The test-crack

issuing from the tip of the notch propagating perpendicular to pre-existing microstructural fabric orientation in Stanstead granite; note the deflection of the test-crack by the grain boundary weakness planes between biotite and feldspar grain. **d** The test-crack propagating parallel to the pre-existing microstructural fabric orientation in Stanstead granite; note the smoother test-crack profile for both rocks when the test-crack is forced to propagate parallel to microstructural fabric in comparison to the situation when it is propagating perpendicular to microstructural fabric. *F* feldspar, *B* biotite, *Q* quartz

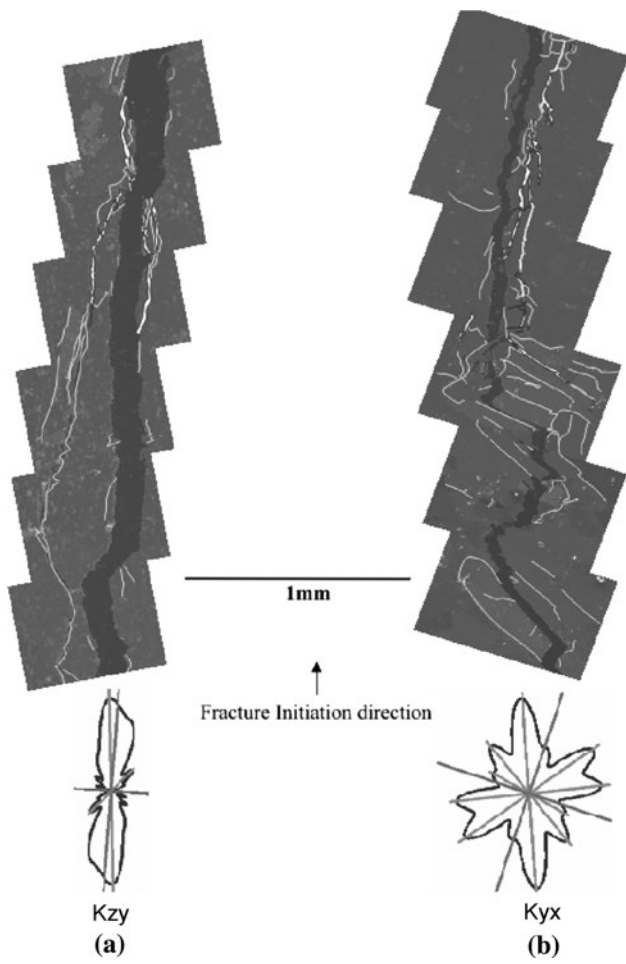


Fig. 9 Comparison of induced microfracture geometry and distribution (traced in white), orientation and the test-crack path (in black color) morphology in Barre granite between **a** when the test-crack is forced to propagate parallel to pre-existing microstructural fabric, in Kzy and **b** when the test-crack is forced to propagate perpendicular to pre-existing microstructural fabric, in Kyx. The rose diagrams show the overall orientation direction of induced fractures within the process zones of Barre granite for these two situations

the induced fractures created during the test-crack propagation process.

3.3 Fracture Roughness Anisotropy

Surfaces of Barre (BG) and Stanstead (STG) granite specimens, created during toughness tests, were analyzed with the purpose of estimating value and distribution for the surface roughness and of investigating the relationship between fracture morphology and fracture toughness. As described in detail by Grasselli (2006) for each fracture surface the parameters A_0 , C , and θ_{\max}^* were calculated along different directions all around the average-plane of the fracture in steps of 5 degrees. The values of θ_{\max}^*/C ratio, obtained for each plane, are plotted as polar diagrams (Figs. 11, 12).

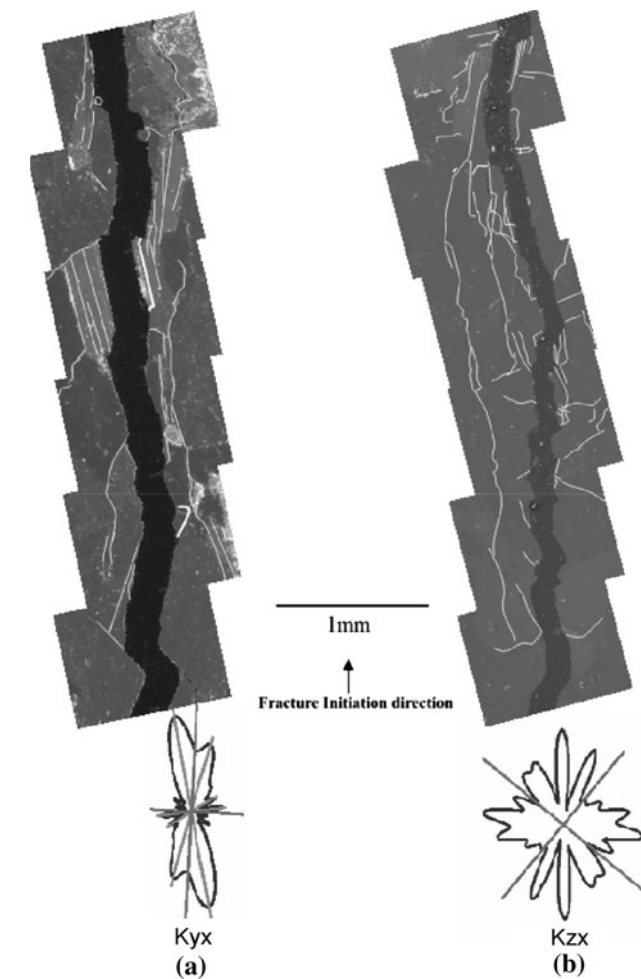


Fig. 10 Comparison of induced microfracture geometry and distribution (traced in white), orientation and the test-crack path (in black color) morphology in Stanstead granite between **a** when the test-crack is forced to propagate parallel to pre-existing microstructural fabric, in Kyx and **b** When the test-crack is forced to propagate perpendicular to pre-existing microstructural fabric, in kzx. The rose diagrams show the overall orientation direction of induced fractures within the process zones of Stanstead granite for these two situations

The comparison among fractures created from the same sample, but along different planes, shows that average roughness values for both Barre and Stanstead granites change as a function of the chosen plane. When the fracture propagates in a plane perpendicular to the pre-existing microstructural petrofabric orientation (samples BGKyx and STKzx) the surface has a greater roughness value with respect to the one measured on samples where the test-crack was forced to propagate parallel to the pre-existing microstructural petrofabric (samples BGKzy and STKyz).

The difference in grain size between the two granites is reflected in the magnitude of roughness values. When comparing Barre tested fracture planes (Fig. 11) with those

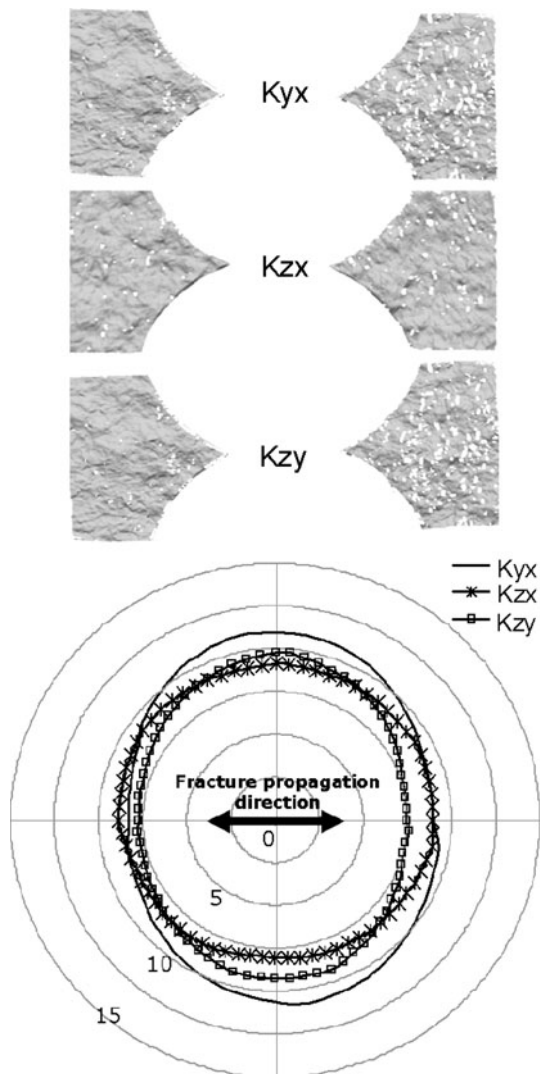


Fig. 11 Surface reconstruction and polar distribution of roughness values (θ_{\max}^*/C) for three surfaces created during cracked chevron notched Brazilian tests on Barre granite samples

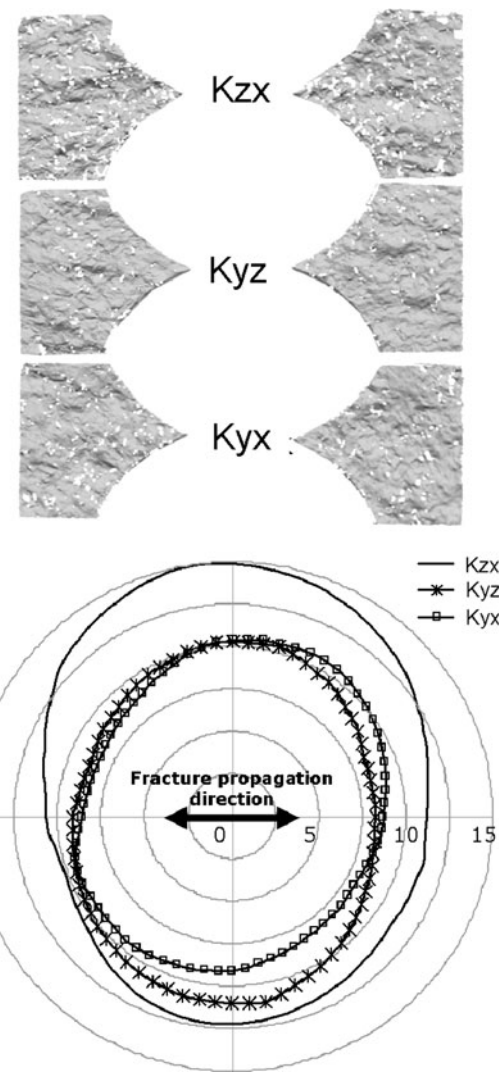


Fig. 12 Surface reconstruction and polar distribution of roughness values (θ_{\max}^*/C) for three surfaces created during cracked chevron notched Brazilian tests on Stanstead granite samples

in Stanstead granite (Fig. 12), all created by forcing the test-crack to propagate at the same angle with respect to the pre-existing microstructural petrofabric, we notice that Stanstead fractured planes are always characterized by greater roughness than Barre granite ones. Observing the profile of the test-cracks on thin sections (Fig. 8a, c), those that are forced to propagate perpendicularly to the pre-existent microstructural petrofabric, mostly follow grain boundaries; therefore, they tend to generate surfaces whose roughness is directly influenced by those fabrics. This could explain why, when comparing the two granites; we observe that the larger grain size for Stanstead granite is also reflected in generally greater roughness and in a higher relative increasing in roughness among the three tested planes compared to the Barre samples (Table 4).

3.4 Characteristic Features of Fracture Process/Damage Zone Using X-ray CT Scan in Barre Granite

To further assess the role of pre-existing 3D microstructural fabric on characteristic features of fracture damage process, a high-resolution micro-CT scanning system has been employed on a Barre granite sample. This involved 3D scanning of the certain volume for the cracked region ($35 \times 25 \times 10$ mm) for both situations where the test-crack was forced to propagate parallel and perpendicular to pre-existing microstructural petrofabric orientation. About 1,000 slices were prepared along three orthogonal planes in Barre granite to examine the role of micro-structure on the characteristics damaged adjacent to the test crack.

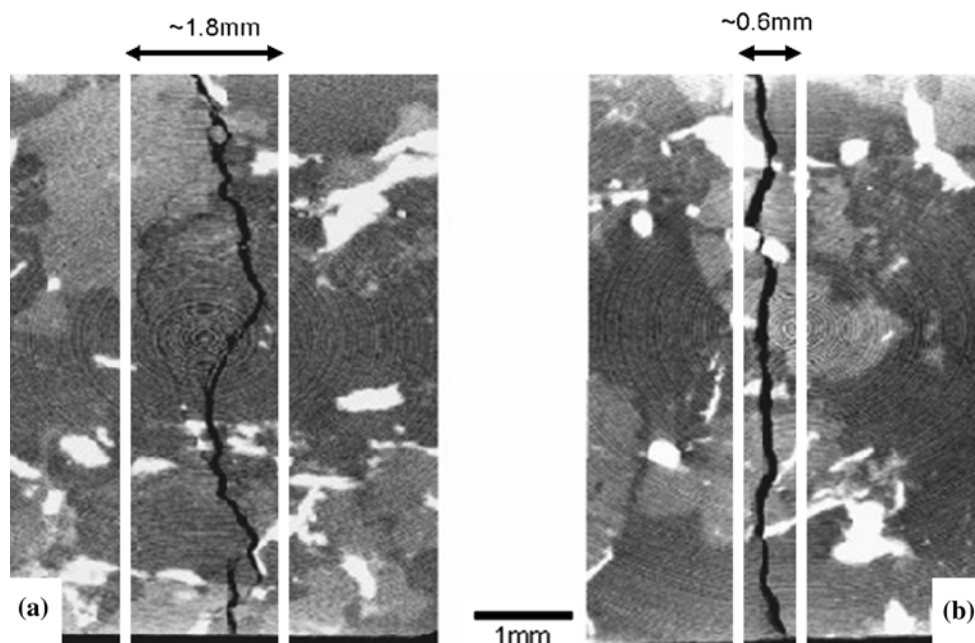


Fig. 13 **a** Traces or profile of micro-CT image of the process zone caused by Kyx sample ($K_{IC} = 1.89 \text{ MPa m}^{0.5}$) when the test-crack is forced to propagate perpendicular to that of the preferred micro-fabric orientation in Barre granite. The width of the process zone at the center of the image is approximately 1.8 mm and the propagation of the crack results in a rough profile. Note the secondary thinner cracks present at the left-hand side of the test-crack. **b** Traces or profile of

micro-CT image of the process zone caused by Kzy sample ($K_{IC} = 1.15 \text{ MPa m}^{0.5}$) when the test-crack is forced to propagate parallel to the preferred micro-fabric orientation. Along this direction bifurcation of the test-crack has not been observed and it follows a relatively smooth profile. The width of the process zone is approximately 0.6 mm

Hoagland et al. (1973) postulated that a “process zone” is generated in the vicinity of a propagating macrocrack tip. The geometry of the process zone of a tensile crack was first calculated by Evans et al. (1977). The fracture process zone in rocks (FPZ) is thus defined as the region affected by microcracking and frictional slip surrounding the visible crack tip propagation under stress (Labuz et al. 1987; Zang and Christian Wagner 2000). The presence of the fracture process zone can be identified as a damaged area surrounding the test-crack. The width of FPZ is considered to be a material property and it was found to increase with increasing grain size (Ouchterlony 1980). The damage observed in the reconstructed images can be identified as the “imprint” of the fracture process zone that moved through the sample during the propagation of the test crack. The analysis shows that the width of the measured fracture process zone correlates well with rock microstructural fabric orientation and fracture toughness values. The micro-CT reconstructed images clearly show that the fracture process zone is much wider (1.8 mm) when the test-crack is forced to propagate perpendicular to the dominant microstructural petrofabric orientation (Fig. 13a), compared to its width (0.6 mm) when the test-crack propagates parallel to the preferred microstructural fabric (Fig. 13b). In the first case the crack follows a tortuous path, exhibits branching, and is characterized with the highest fracture toughness

value ($1.89 \text{ MPa m}^{0.5}$). On the contrary, in the second case, the crack follows a more linear path and is characterized with the lowest fracture toughness value ($1.15 \text{ MPa m}^{0.5}$).

4 Discussion

In this study an attempt is made to correlate fracture roughness with fracture toughness (mode I) obtained along specific planes in two granitic rocks that are characterized by different microstructural properties. Barre granite is finer in grain size and shows aligned preferred microcracks and mineral fabric orientations, and reveals higher average K_{IC} (i.e. $1.49 \text{ MPa m}^{0.5}$) than what is observed in Stanstead granite (i.e. $1.13 \text{ MPa m}^{0.5}$), which is coarser and lacks alignment between the preferred microcracks and mineral fabrics within the three orthogonal planes studied (Nasseri et al. 2005). Barre granite also shows slightly higher fracture toughness anisotropy (1.64) than Stanstead (1.53). Both rocks show a correlation between fracture roughness values and their associated fracture toughness (Fig. 14). The fracture roughness values obtained from fracture surfaces in Stanstead granite are higher than those obtained from fracture surfaces in Barre granite. SEM images from thin sections show that for both granites, the test-crack generally propagates following micro-fabric structures.

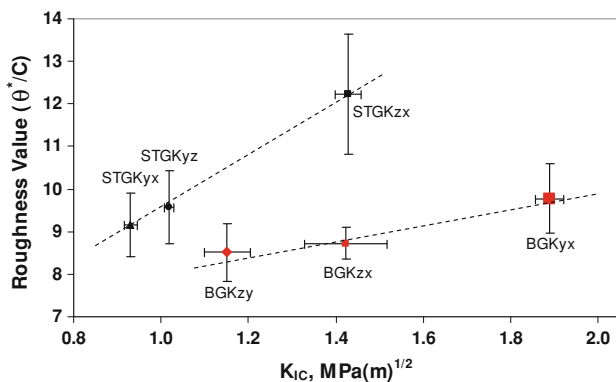


Fig. 14 Variation of fracture toughness with fracture roughness in Barre and Stanstead granites

This suggests that the difference in roughness between Barre and Stanstead granite is also influenced by the larger microstructural features, such as grain size. Interestingly, the roughness measured in BGK_{yx} plane proves to be larger than STG_{Kyz} and STG_{Kyx} . These experimental observations suggest that the relative importance of grain size and micro-structure orientation in the measured values of fracture toughness and roughness has to be taken into consideration. Specific orientation of micro-crack alignment could result in frequent out-of-plane propagation of the test-crack irrespective of grain-size distribution. The higher measured value of roughness for BGK_{yx} than either STG_{Kyz} or STG_{Kyx} , despite the latter's relative coarseness supports this argument (Fig. 9b). We have also observed that all measured fracture surfaces, independent of rock type; show an anisotropic roughness (elliptical curves in Figs. 11, 12) with higher roughness values in the direction perpendicular to the fracture propagation. This result suggests that the fracturing process and its direction of propagation could be responsible for anisotropy in fracture roughness, leading to the creation of a preferential direction for shear displacements and fluid flow.

5 Conclusion

The results presented in this paper confirm the essential link among petrofabric anisotropy, fracture toughness, fracture roughness, and evolution and extent of associated induced cracks along specific directions in the process zone of the two rocks studied. Both rocks showed a significant increase of K_{IC} (53% to 64%) and fracture roughness (15% to 34%) between directions parallel to and normal to petrofabric orientation. The failed specimens show a positive relationship between their measured fracture toughness and fracture roughness. Stanstead granite being characterized by a coarser microstructural fabric shows a rougher surface in comparison to Barre granite.

The study also highlights the need for employment of advanced post-failure diagnostic techniques in quantifying the interrelationships between the microstructural anisotropy and fracture process zone dimensions, and the geometry of induced fractures within it.

Acknowledgments The authors wish to thank Dr. SH Cho and his associates for their assistance in the CT-scan work, Dr J. Wirth and Mr. M. Braun for their assistance with the surface scans. The research work has been partially supported by NSERC/Discovery Grant No. 341275 and NSERC/RTI Grant No. 345516.

References

- Backers T, Fardin N, Dresen G, Stephansson O (2003) Effect of loading rate on mode I fracture toughness, roughness and micromechanics of sandstone. *Int J Rock Mech Min Sci* 40:425–433
- Grasselli G (2001) Shear strength of rock joints based on quantified surface description. Ph.D. thesis, Swiss Federal Institute of Technology (EPFL), Lausanne, Switzerland, 125 p
- Grasselli G (2006) Manuel Rocha Medal recipient—Shear strength of rock joints based on quantified surface description. *Rock Mech Rock Eng* 39:295–314
- Grasselli G, Wirth J, Egger P (2002) Quantitative three-dimensional description of a rough surface and parameter evolution with shearing. *Int J Rock Mech Min Sci* 39:789–800
- Hoagland RG, Hahn GT, Rosenfield AR (1973) Influence of microstructure on fracture propagation in rock. *Rock Mech* 5:77–106
- Iqbal N, Mohanty B (2006) Experimental calibration of stress intensity factors of the ISRM suggested cracked chevron-notched Brazilian disc specimen used for determination of mode-I fracture toughness. *Int J Rock Mech Min Sci* 43:1270–1276
- ISRM (1995) Suggested methods for the determining mode I fracture toughness using cracked chevron notched Brazilian disc (CCNBD) specimens. *Int J Rock Mech Min Sci Geomech Abstr* 32:57–64
- Issa MA, Issa MA, Islam MS, Chudnovsky A (2003) Fractal dimension—a measure of fracture roughness and toughness of concrete. *Eng Fract Mech* 70:125–137
- Labuz JF, Shah SP, Dowding CH (1987) The fracture process zone in granite: evidence and effect. *Int J Rock Mech Geomech Abstr* 24(4):235–246
- Lange DA, Jennings HM, Shah SP (1993) Relationship between fracture surface-roughness and fracture-behavior of cement paste and mortar. *J Am Ceram Soc* 76:589–597
- Launeau P, Robin PYF (1996) Fabric analysis using the intercept method. *Tectonophysics* 267:91–119
- Nasseri MHB, Mohanty B (2008) Fracture toughness anisotropy in granitic rocks. *Int J Rock Mech Min Sci* 45:167–193
- Nasseri MHB, Mohanty B, Robin PYF (2005) Characterization of microstructures and fracture toughness in five granitic rocks. *Int J Rock Mech Min Sci* 42:450–460
- Nasseri MHB, Mohanty B, Young RP (2006) Fracture toughness measurements and acoustic emission activity in brittle rocks. *Pure Appl Geophys* 163:917–945
- Ouchterlony F (1980) Review of fracture toughness testing of rocks. DS 1980 15, Swed Detoic Res Found Stockholm
- Wirth J (2002) Rapid modeling. Hanser, Munich, p 220
- Zang A, Christian Wagner F (2000) Fracture process zone in granite. *JGR* 105(B10):23651–23661